



Cyclotron resonance in ferromagnetic InMnAs and InMnSb

G. A. Khodaparast,^{1,*} Y. H. Matsuda,² D. Saha,³ G. D. Sanders,³ C. J. Stanton,³ H. Saito,² S. Takeyama,² T. R. Merritt,¹ C. Feeser,⁴ B. W. Wessels,⁴ X. Liu,⁵ and J. Furdyna⁵

¹*Department of Physics, Virginia Tech, Blacksburg, Virginia 24061, USA*

²*Institute for Solid State Physics, University of Tokyo, Kashiwanoha, Kashiwa, Chiba 277-8581, Japan*

³*Department of Physics, University of Florida, Gainesville, Florida 32611, USA*

⁴*Materials Research Center, Northwestern University, Evanston, Illinois 60208, USA*

⁵*Department of Physics, University of Notre Dame, Notre Dame, Indiana 46556, USA*

(Received 24 July 2013; revised manuscript received 21 October 2013; published 11 December 2013)

We present experimental and theoretical studies of the magneto-optical properties of p -type $\text{In}_{1-x}\text{Mn}_x\text{As}$ and $\text{In}_{1-x}\text{Mn}_x\text{Sb}$ ferromagnetic semiconductor films in ultrahigh magnetic fields oriented along [001]. Samples were fabricated by molecular beam epitaxy (MBE) and metal-organic vapor phase epitaxy (MOVPE). To model the results, we used an 8-band Pidgeon-Brown model generalized to include the wave vector dependence of the electronic states along k_z as well as the s - d and p - d exchange interactions with the localized Mn d electrons. The Curie temperature is taken as an input parameter and the average Mn spin is treated in mean-field theory. We compared Landau level and band structure calculations with observed cyclotron resonance (CR) measurements. While differences between the CR measurements are seen for MBE and MOVPE samples, our calculations indicate that they arise from differences in the carrier densities. In addition, the difference in the carrier densities suggests significantly larger average spin for the MOVPE structures; this fact could be responsible for higher Curie temperatures in this material system.

DOI: [10.1103/PhysRevB.88.235204](https://doi.org/10.1103/PhysRevB.88.235204)

PACS number(s): 75.50.Pp, 76.40.+b, 71.18.+y, 07.55.Db

I. INTRODUCTION

Carrier-induced ferromagnetism in dilute magnetic III-V semiconductors¹⁻⁴ has opened up several opportunities for device applications, as well as fundamental studies of a material system in which itinerant carriers interact with the localized spins of magnetic impurities. The origin of carrier-induced ferromagnetism is still controversial. Reasonable agreement between theory and experiment has been noted for molecular beam epitaxy (MBE) grown GaMnAs but, in contrast, the Curie temperatures (T_c) of MBE-grown InMnAs films are inconsistent with theory.⁷⁻⁹ Based on theoretical calculations, InMnAs with a hole concentration of 10^{19} – 10^{20} cm^{-3} should have a T_c of 8 K instead of the experimentally observed 40–90 K for MBE samples.² The case for metal-organic vapor phase epitaxy (MOVPE) grown films is even more complex. Films with a carrier concentration of 10^{18} cm^{-3} have a T_c of 330 K and this T_c is nearly independent of carrier concentration.^{7,8}

Cyclotron resonance (CR) spectroscopy is an extremely powerful tool for the study of electronic states in semiconductors. In this paper we compare the experimental and theoretical studies of the magneto-optical properties of p -type MBE and MOVPE $\text{In}_{1-x}\text{Mn}_x\text{As}$ and $\text{In}_{1-x}\text{Mn}_x\text{Sb}$ ferromagnetic semiconductor films in ultrahigh magnetic fields oriented along [001]. To model the CR, we use an 8-band Pidgeon-Brown model generalized to include the wave vector dependence of the electronic states along k_z as well as the s - d and p - d exchange interactions with the localized Mn d electrons. The Curie temperature is taken as an input parameter and the average Mn spin is treated in mean-field theory.^{10,11} While CR has been used to study MBE-grown ferromagnetic InMnAs with a GaSb buffer layer on a GaAs substrate with T_c ranging from 30 to 50 K,¹² the CR in the these MBE-grown ferromagnetic structures had features significantly different

from the ones reported in this work. Because the InMnAs/GaSb interface is a type-II interface, with electrons and holes confined on opposite sides of the heterojunction, it is possible that in the MBE-grown InMnAs structures, the CR could have originated from or been influenced by carriers at the interface layer between InMnAs and GaSb.¹² In contrast, in this study, MOVPE InMnAs samples were grown directly on GaAs and our results provide a more direct probe of the CR in this family of the ferromagnetic films and interface effects should be minimal. In addition, in this study we observe the CR of holes in InMnSb. These observations should be contrasted to those of ferromagnetic GaMnAs where no observable CR has been seen to date, even for magnetic fields in the megagauss range. Several groups have reported that the optical conductivity in GaMnAs shows non-Drude-type behavior¹³⁻¹⁶ while InMnAs and InMnSb both clearly show Drude-type conductivity.¹⁷⁻²⁰ In addition, a scanning tunneling microscopy study revealed the d -wave envelope function in the acceptor state in GaMnAs.¹⁶ These facts indicate that holes in InMnAs and InMnSb could have different characteristics than holes in GaMnAs. Furthermore, the clear observation of hole CR in our ferromagnetic narrow-gap structures suggests the existence of *delocalized* holes. Tuning of the excitation wavelength in this study allowed us to probe several possible Landau level transitions in the nonparabolic valence band, demonstrating a strong mixing of the heavy and light hole bands that contributes to the hole effective mass. In our model, the total effective mass Hamiltonian is the sum of the Landau, Zeeman, and sp - d exchange interaction Hamiltonians.

Since these magnetic semiconductors usually have low carrier mobilities [typically on the order of $100 \text{ cm}^2/(\text{Vs})$], a very high magnetic field is necessary to observe CR, i.e., $\omega_c \tau > 1$, where ω_c is the cyclotron frequency. Due to the fact that CR directly provides the carrier effective masses and scattering times, we can obtain detailed information

TABLE I. Characteristics of the samples studied in this work. The carrier density and mobility are extracted from the Hall measurements.

Sample	Growth Method	Density (cm ⁻³)	Film Thickness (nm)	x (%)	T_c (K)
InMnAs	MOVPE	1.35×10^{18}	600	4	330
InMnAs	MOVPE	1.6×10^{18}	235	2	330
InMnAs	MOVPE	4.8×10^{18}	970	1	330
InMnSb	MOVPE	1.9×10^{18}	500	5.6	590
InMnSb (A)	MBE	3.0×10^{20}	230	2	10
InMnSb (B)	MBE	1.0×10^{20}	230	2	10

on the itinerancy of the carriers. In contrast, the effective masses and scattering times are normally difficult to deduce independently in transport measurements. In addition, our observations provide information on the band structure, the $sp-d$ exchange parameters (α and β), the average spin as a function of the hole density, and the position of the Fermi level in these material systems.

In this paper, we present our experimental results for CR in InMnAs and InMnSb samples grown by MBE and MOVPE and compare the results with theoretical calculations. We find differences between the position of the CR resonances for MBE vs MOVPE samples. Our calculations agree reasonably well with the experiments and show that differences between CR in the MBE and MOVPE samples are primarily due to different carrier densities in the two types of samples. In addition, we find that the MOVPE samples typically have narrower linewidths than the MBE samples which is consistent with the MOVPE samples having lower carrier densities.

This paper is organized as follows. In Sec. II, we discuss the characteristics of the samples studied in this work; in Sec. III, we discuss the experimental results; in Sec. IV, we present and discuss our theoretical modeling; and in Sec. V the results will be discussed.

II. SAMPLES

One In_{1-x}Mn_xSb and three In_{1-x}Mn_xAs films were grown by MOVPE at Northwestern University and two In_{1-x}Mn_xSb films with 2% Mn content were grown at the University of Notre Dame by low-temperature MBE.^{5,6} The samples' characteristics are summarized in Table I and the details of their growth are described elsewhere.⁵⁻⁸ The carrier density and mobility are extracted from the Hall measurements. The carrier densities were used as input to define the position of the Fermi levels. The extracted CR mobilities from the line shapes are much higher than the dc Hall mobilities.

III. EXPERIMENTAL CR MEASUREMENTS

CR measurements were performed using CO₂, H₂O, and CO lasers, providing laser radiation at 10.6, 10.7, 16.9, and 5.53 μ m. External magnetic fields exceeding 100 T were generated by a single-turn coil technique.¹⁰ The magnetic field was applied along the growth direction and measured by a pickup coil around the sample which was placed inside a continuous-flow helium cryostat. Several IR wavelengths were used as the excitation source and the transmitted

signal through the sample was collected using either a fast liquid-nitrogen-cooled HgCdTe detector or a Cu-doped Ge detector. A multichannel digitizer placed in a shielded room recorded the signals from the detector and the pickup coil. Although the single-turn coil is destroyed in each shot, the sample and pickup coil remain intact, making it possible to carry out detailed temperature and wavelength dependent measurements on the same sample. Since the transmission signal can be recorded during both the up and down sweeps, each CR resonance was observed twice in a single pulse. This fact allowed us to check the reproducibility of the observed resonance peaks and to make sure that the spectra were free from any slow heating effects.¹⁰ The transmission measurements presented here are ratios of the field-dependent transmission relative to the transmission at zero magnetic field, $T(B)/T(B=0)$.

Figure 1 shows the CR measurements for MBE-grown InMnSb (sample A, in Table I) and MOVPE-grown InMnAs in Table I, both with Mn contents of 2% Mn. For the same Mn content, the MBE-grown InMnSb sample has a greater hole density than the MOVPE-grown InMnAs sample. This is evidenced by the fact that the InMnSb (A) sample has a larger cyclotron mass than the MOVPE-grown InMnAs sample. The larger hole density and Fermi energy are associated with CR originating from Landau level transitions at higher magnetic fields thereby enhancing the cyclotron mass. The hole CR in InMnSb has been observed for the first time, and in the case of Fig. 1(a), the CR masses are $0.057m_0$ at room temperature and $0.051m_0$ at 121 K. These are much smaller than the band edge HH mass in InSb ($0.32m_0$). The theoretical CR absorption spectra in Fig. 1(b) are obtained from magneto-optical absorption due to transitions between different Landau levels. From Fermi's golden rule, the magneto-optical absorption coefficients at a given photon energy for magnetic fields perpendicular to the sample can be calculated. The details of our calculations are described in the theory section of this paper.

In order to demonstrate the effect of Mn content on the electronic band structure of InMnAs and InMnSb, we calculated the energy levels as a function of magnetic field and Mn content. The results are shown in Fig. 2 where we plot the zone-center Landau valance subband energies as functions of the applied magnetic field for Mn contents ranging from zero to 4%. Details of the calculations will be described more fully in Sec. IV. The valance subband energies at the top of the valance band are strongly modified by increasing the Mn content. The color coding of the states gives the Pidgeon-Brown manifold numbers ranging from -1 to 4 (discussed more fully in Sec. IV) and aids in classifying the states. It is important to note that the topmost Landau level, indicated by the blue line, is the heavy-hole spin-down state (corresponding to the -1 Pidgeon-Brown manifold) and is a pure spin state with a Mn content of 2% from 0–80 T and from 0–120 T for 4% Mn. We can readily see the differences between the InMnAs material and the InMnSb material. In addition, we also see the effect of adding Mn. The most notable effect of adding Mn is to push the heavy-hole spin-down PB = -1 Landau level up.

Figure 3(a) shows the calculated total CR transmission, as well as contributions to the CR transmission due to transitions between two Landau levels with different Pidgeon-Brown (PB)

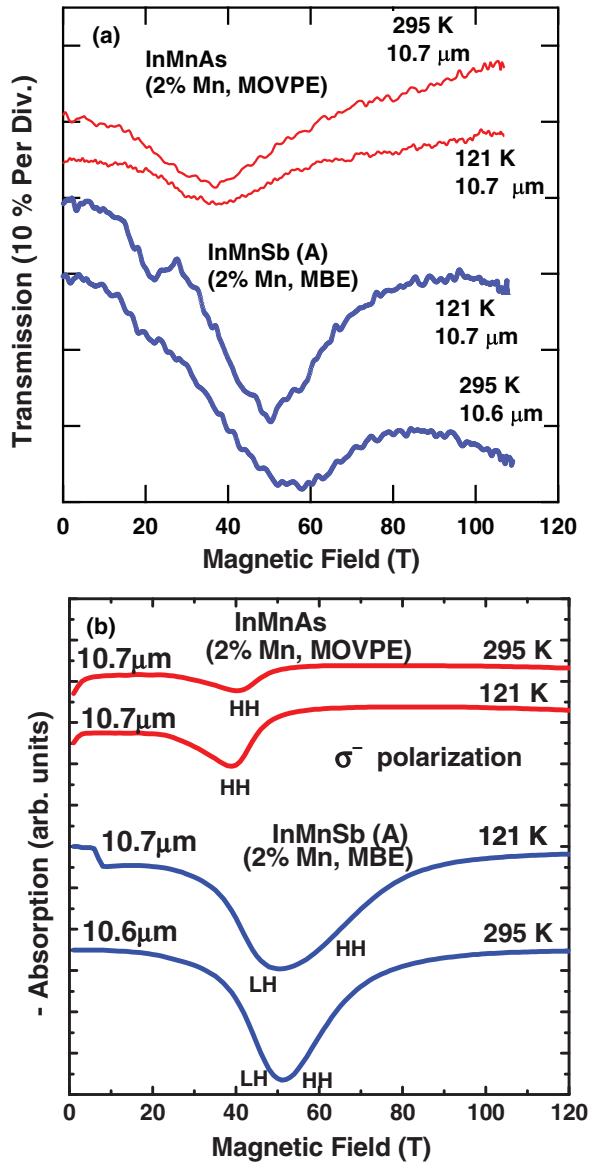


FIG. 1. (Color online) (a) CR spectra for InMnAs and InMnSb films. The CR of InMnSb at 295 K was measured at $10.6 \mu\text{m}$, while the other three resonances were measured at $10.7 \mu\text{m}$. (b) Comparing calculated CR spectra for InMnAs and InMnSb to the experimental results in (a). The CR resonance in InMnAs originates from a single (HH only) transition, while in InMnSb it arises from multiple (both LH and HH) transitions. In the case of the InMnSb, a better fit to experimental data was generated for a hole density of $3.0 \times 10^{20} \text{ cm}^{-3}$.

manifold indices $(-1, 0, 1, 2, 3, 4, \dots)$, for the measurement in Fig. 1(a). Figure 3(b) shows Landau level calculations for the CR transitions in InMnSb arising from both LH and HH transitions. In Fig. 3(b), each color (online) represents a Landau level with a specific PB manifold index $(-1, 0, 1, 2, \dots)$ and the Fermi energy is shown as a red dashed line. We also use the notation (p, q) to denote the Landau levels which are responsible for the transitions, where p corresponds to the PB manifold index and q represents the state within the manifold in order of increasing energy. In this paper, we will maintain the same conventions of notations for all the upcoming figures

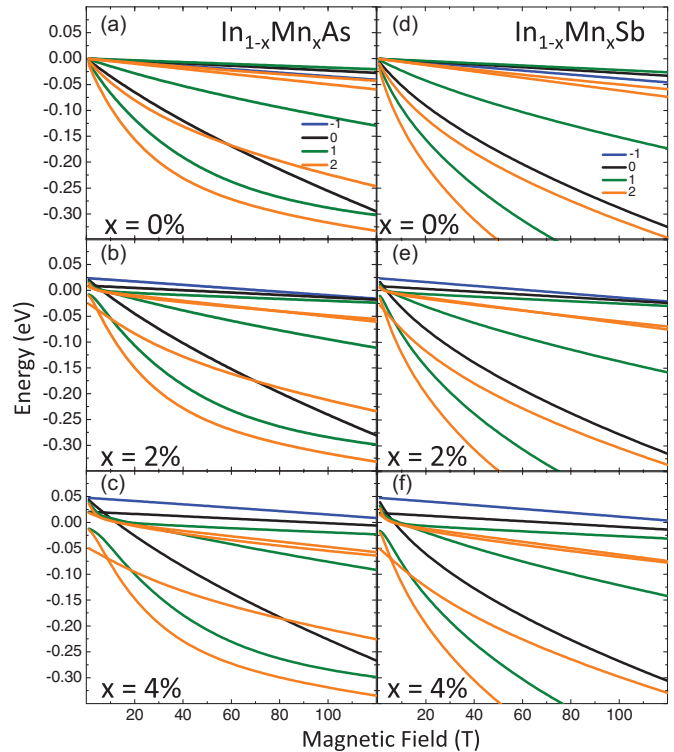


FIG. 2. (Color online) Zone-center Landau valance subband energies (at $T = 121 \text{ K}$ and $T_c = 330 \text{ K}$) as functions of magnetic field in $\text{In}_{1-x}\text{Mn}_x\text{As}$ and $\text{In}_{1-x}\text{Mn}_x\text{Sb}$ for different Mn concentrations (x). The color coding gives the Pidgeon-Brown manifold number and helps us to identify the states.

similarly to Fig. 3. As shown in Fig. 4 from a different perspective, for a fixed magnetic field of 47 T where several CR transitions have been observed, the band mixing between different manifold decreases with increasing Mn content.

In order to probe the CR in different magnetic field regions, the CR spectra were measured in InMnAs and InMnSb at wavelengths $16.9 \mu\text{m}$ and $5.53 \mu\text{m}$. Figure 5 shows the measurements at $16.9 \mu\text{m}$ where the resonance feature of InMnAs is less clear than that found at 10.6 and $10.7 \mu\text{m}$. This can be attributed to the low-mobility of the sample and the plasma absorption effect. For InMnSb, the resonance pattern is unlike a typical single-resonance peak. According to our Landau level calculations, the overlap of light-hole and heavy-hole resonances can result in such unusual CR spectra.

Figure 6(a) shows the CR spectra at $5.53 \mu\text{m}$ for the three MOVPE-grown InMnAs samples with different Mn contents. The samples with the lowest Mn content have a nonsymmetric resonance line shape which is expected for samples with low carrier mobilities. With increasing Mn content, the position of the CR peak shifts to higher magnetic fields while the line broadening decreases, which can be reflected as a higher CR mobility [$\sim 750 \text{ cm}^2/(\text{V s})$] in the sample with 4% Mn content compared to the other two samples. The area under the curve of the CR traces is related to the hole concentration, where tuning the Mn content from 2% to 4% did not significantly increase the hole concentration for the samples here. This fact may be related to the lack of variations in the T_c with small variations in the Mn content. The increase in

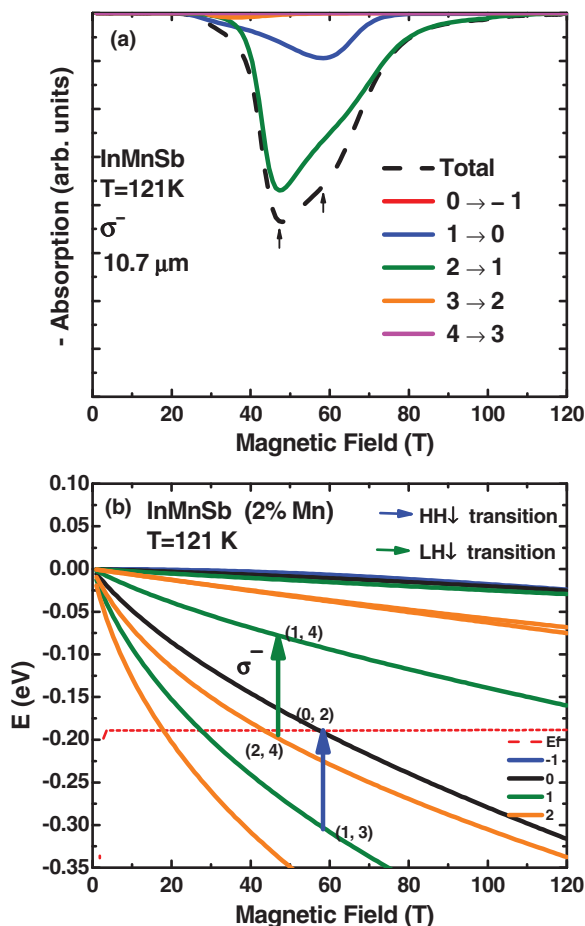


FIG. 3. (Color online) (a) Total transmission calculated for the CR observation of InMnSb at $10.7 \mu\text{m}$. (b) Zone-center Landau valance subband energies at $T = 121 \text{ K}$ as functions of magnetic field in p -doped InMnSb. The Fermi energy is shown for the hole concentration, $p = 1 \times 10^{20} \text{ cm}^{-3}$.

the hole concentration with increasing Mn content has been attributed to an enhanced exchange interaction. The Landau level calculations predict the positions of the CR peaks in all three samples, presented in Fig. 6(b) for InMnAs with 4% Mn and in Fig. 7 for the other two samples.

We examined CR for $5.53 \mu\text{m}$ excitation for one MOVPE-grown and two MBE-grown InMnSb films. The CR of the MOVPE-grown film at this wavelength was observed only at low temperatures, similarly to the case for the InMnAs film shown in Fig. 6(a). As shown in Fig. 8 for MOVPE-grown InMnSb, two resonances were observed and Fig. 9(a) presents the Landau level calculations that relate the origin of the strong resonance to the HH transition. The band structure calculation in Fig. 9(b) shows the possible transitions for the weak resonance at 20 Tesla.

In Fig. 10 we see features that are attributable to electron CR at room temperature for MBE-grown InMnSb, sample (B), with a hole density of $\sim 1.0 \times 10^{20} \text{ cm}^{-3}$. CR transitions are observed for σ^+ circular polarization while, for a free hole gas, CR occurs only for σ^- circular polarization. As a result, CR in σ^+ polarization is often called electron-active (e-active) and σ^- polarization is referred to as hole-active (h-active). The situation in real semiconductors differs from that in a gas of

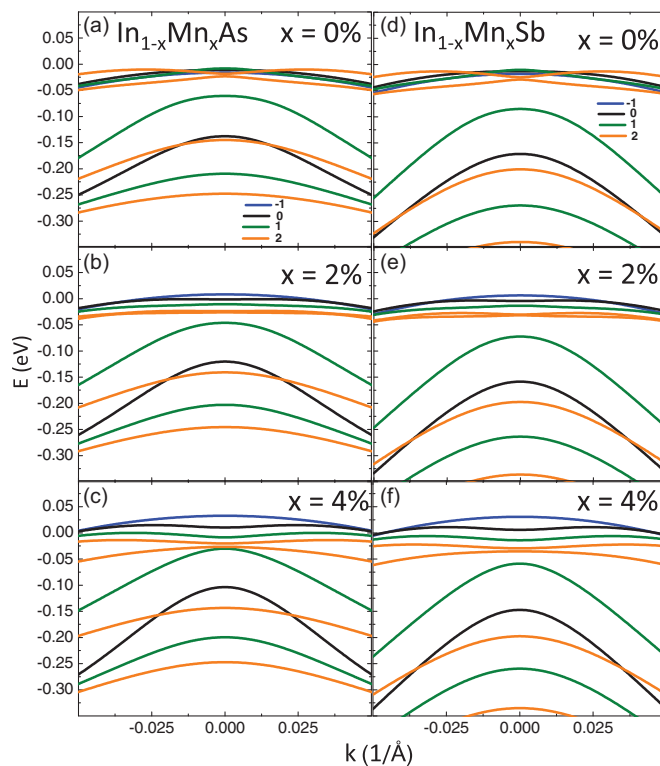


FIG. 4. (Color online) Valance band structure at $B = 47 \text{ T}$ (with $T = 121 \text{ K}$ and $T_c = 330 \text{ K}$) in $\text{In}_{1-x}\text{Mn}_x\text{As}$ and $\text{In}_{1-x}\text{Mn}_x\text{Sb}$ for different Mn concentrations (x). The topmost level evolves as a pure spin state by increasing the Mn content.

free positive or negative carriers. Recently, e-active CR in p -doped InAs and InMnAs has been reported.¹⁰ The valance band consists of two types of carriers: heavy holes ($J = 3/2, M_j = \pm 3/2$) and light holes ($J = 3/2, M_j = \pm 1/2$). Each of them has their own Landau ladder in a magnetic field. An increase of n always implies a decrease in energy but only within each ladder. Like the conduction band case, transitions within a ladder (HH \rightarrow HH or LH \rightarrow LH) can take place only in h-active (σ^-) polarization. However, the relative position of the two ladders can be such that interladder transitions (LH \rightarrow HH) in e-active polarization are allowed. In addition, considering the large hole concentrations in the MBE-grown InMnSb, and for the temperature where the e-active was observed, the observed e-active CR could have originated from the thermally excited electrons in the conduction band. In our measurements, the e-active CR was not observed at low temperatures or in the the MOVPE-grown samples with much lower hole densities. By comparing the line shape and the width of the resonance in Fig. 10 with the measurements presented in Fig. 8, we conclude that the MOVPE-grown InMnSb has a much higher CR mobility where μ_{CR} of $\sim 1000 \text{ cm}^2/(\text{V s})$ can be estimated. This is due to the higher growth temperature of the MOVPE structures and the resulting reduction in the number of defects.^{7,8} A summary of μ_{CR} in different samples can be found in Table II. The differences in carrier density between the MBE-grown and MOVPE-grown structures could be an important factor in the differences in their Curie temperatures. Recently in GaMnAs, the tunability of the Fermi level within the impurity band is considered to

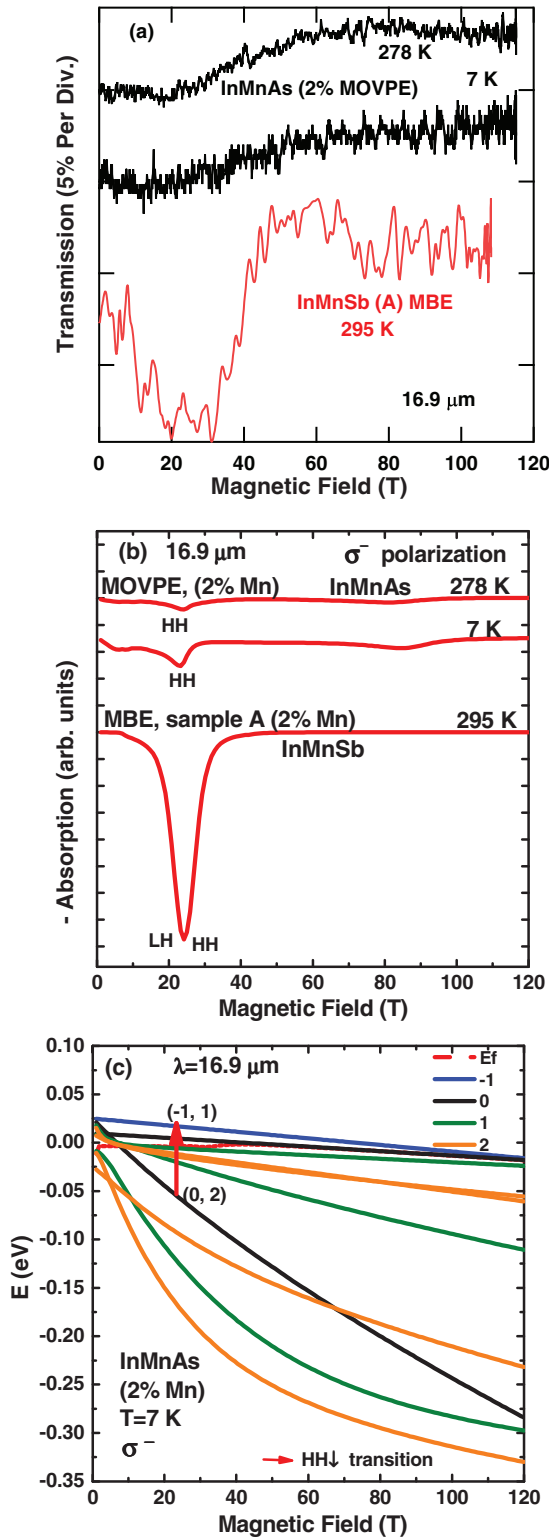


FIG. 5. (Color online) (a) Cyclotron resonance spectra in InMnAs and InMnSb at 16.9 μm. (b) Calculated CR spectra for InMnAs and InMnSb from the experimental results in (a). The CR in InMnAs originates from a single (HH only) transition, while in InMnSb it arises from multiple (both LH and HH) transitions, as shown in Fig. 3(b). (c) The Landau level calculation at $T = 7$ K as functions of magnetic field in p -doped InMnAs demonstrates only one possible transition. The Fermi energy is shown for the hole concentration, $p = 2 \times 10^{18} \text{ cm}^{-3}$.

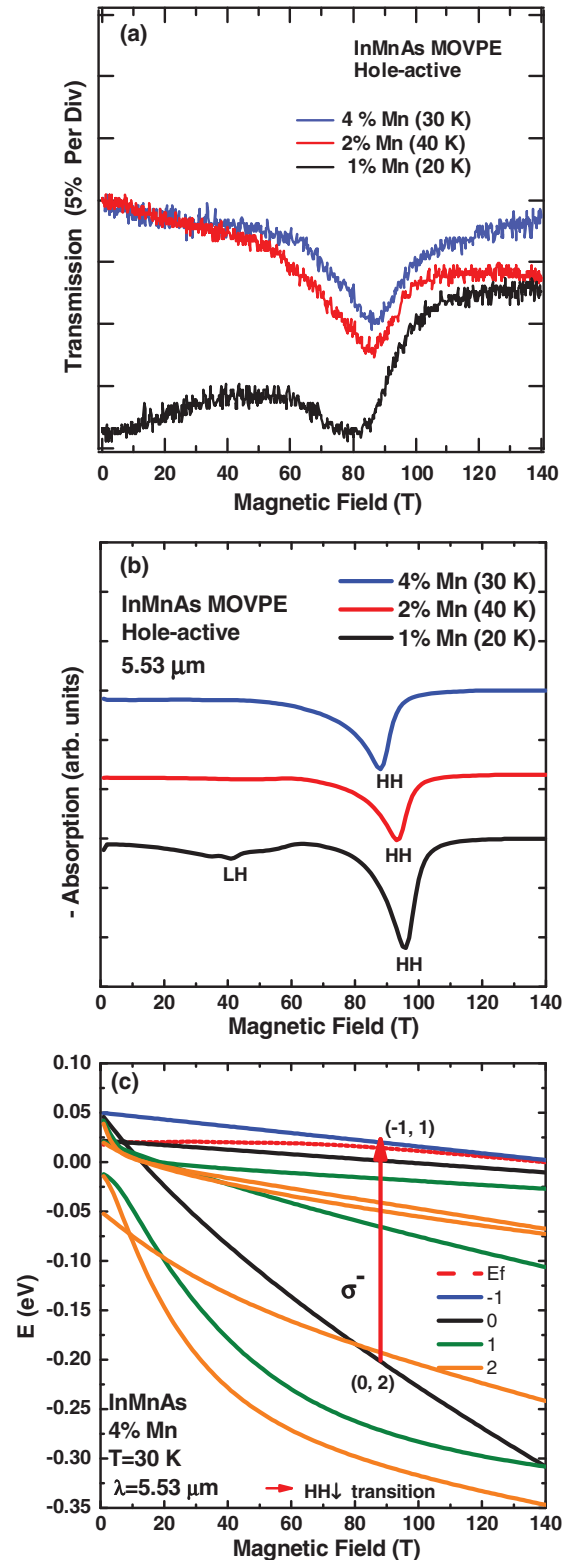


FIG. 6. (Color online) (a) Cyclotron resonance spectra in InMnAs at 5.53 μm using the hole-active circular polarization of radiation. Comparing the area under the curve of the CR traces suggests that tuning the Mn content from 2% to 4% does not increase the hole concentrations significantly. (b) Calculated CR spectra for InMnAs corresponding to the experimental results in (a). (c) Calculated Landau levels for InMnAs with 4% Mn content demonstrating one possible CR transition for 5.53 μm excitation.

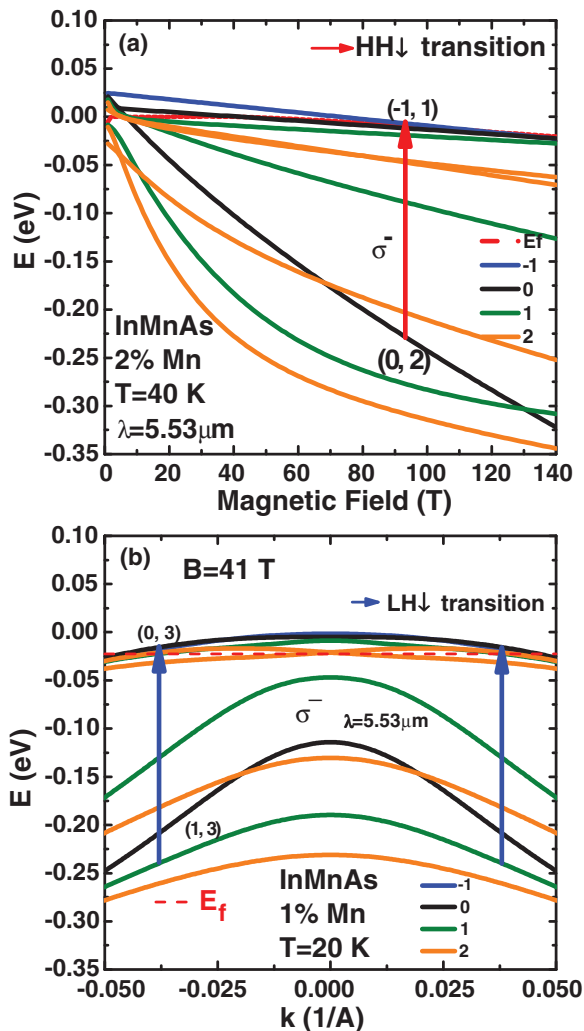


FIG. 7. (Color online) (a) Calculated Landau levels for InMnAs with 2% Mn content, demonstrating one possible CR transition for $5.53 \mu\text{m}$ excitation. (b) Calculated valance band structure for $T = 40 \text{ K}$ and $B = 47 \text{ T}$ in p -doped InMnAs with the weak intersubband transition corresponding to the CR spectrum of InMnAs with 1% Mn content. The Fermi energy is shown for the hole concentration of $p = 4.8 \times 10^{18} \text{ cm}^{-3}$.

define and tune the T_c .²¹ The position of the Fermi level is also important for determining the magnitude of the average spin in ferromagnetic semiconductors. Figures 11(a) and 11(b) show the position of the Fermi level for the MBE-grown InMnSb (A) and MOVPE-grown InMnSb, respectively. The hole density of the MOVPE-grown sample is a factor of 100 smaller than in the MBE structure, which can significantly change the z component of the average spin as shown in Fig. 11(c). This change occurs because in the Pidgeon-Brown model, at low densities, only the lowest energy state [topmost level, shown in blue in Fig. 11(a)] is occupied. This state is a 100% heavy hole down state, which is a pure spin-down state. At higher densities, the Fermi level is in the middle of the valence band states and hence several of the valence band states are occupied [see Fig. 11(b)]. The higher level valence band states are mixtures of heavy and light hole states and as a result, spin is not a good quantum number. In addition, several valence

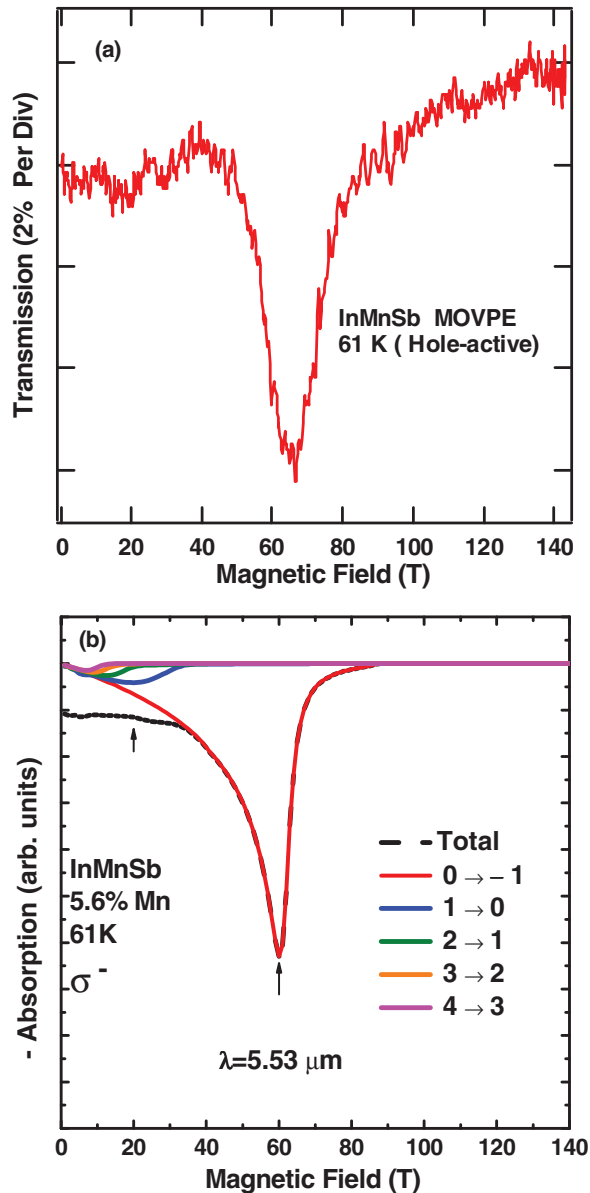


FIG. 8. (Color online) (a) Observed CR for the MOVPE-grown InMnSb. (b) The calculated transmission indicating the two observed resonances, one weak feature around 20 T and a strong resonance around 60 T.

band states are occupied and the average spin polarization goes down.

IV. THEORY AND MODELING

We developed an effective mass theory for CR in bulk narrow-gap dilute magnetic III-V semiconductors such as InMnAs. Details of our effective mass theory are described in Ref. 11. In that paper, we applied our theory to the study of n -type InMnAs alloys and compared our results with experimental CR measurements. We later applied our theory to the analysis of CR magneto-optics in bulk n - and p -type InAs and InMnAs samples in ultrahigh magnetic fields²²⁻²⁴ and demonstrated the use of CR in determining carrier densities in InMnAs.²⁵ Here we outline our theoretical model and refer the

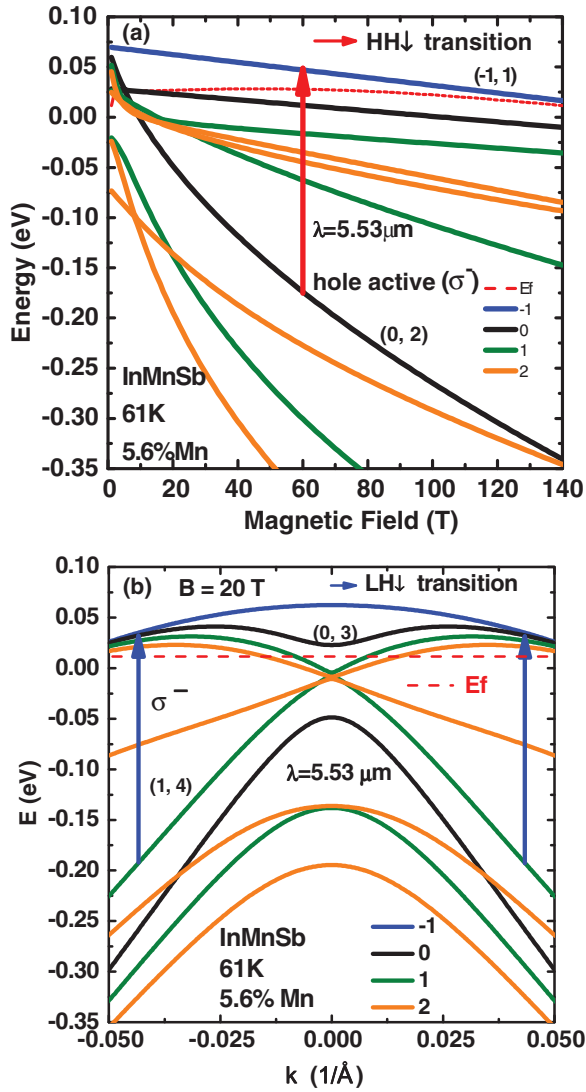


FIG. 9. (Color online) (a) Calculated Landau levels for InMnSb with 5.6% Mn content, demonstrating the strong CR transition for 5.53 μm excitation. (b) Calculated band structure of the p -doped InMnSb for $B = 20$ T with the weak intersubband transition corresponding to the CR spectrum in Fig. 8(a). The wave vector k is in the direction of magnetic field. The Fermi energy is shown for the hole concentration, $p = 1.9 \times 10^{18} \text{ cm}^{-3}$.

interested reader to the more detailed treatments in the above references.

A. Effective mass Hamiltonian

Our model is based on the 8-band $\mathbf{k}\cdot\mathbf{p}$ Pidgeon-Brown model²⁶ for a narrow-gap semiconductor in a static magnetic field parallel to the (001) direction (taken to be the z direction, B_z). In our model, we generalize the Pidgeon-Brown model to include the wave vector (k_z) dependence of the itinerant electronic states as well as the sp - d coupling of the itinerant carriers to the localized d electrons in the Mn ion cores. We use this model to analyze the experimental CR spectra of InMnAs and InMnSb ferromagnetic semiconductor films. Following the original Pidgeon-Brown model, we separate the 8 Bloch basis states into an upper and lower set of 4 Bloch basis

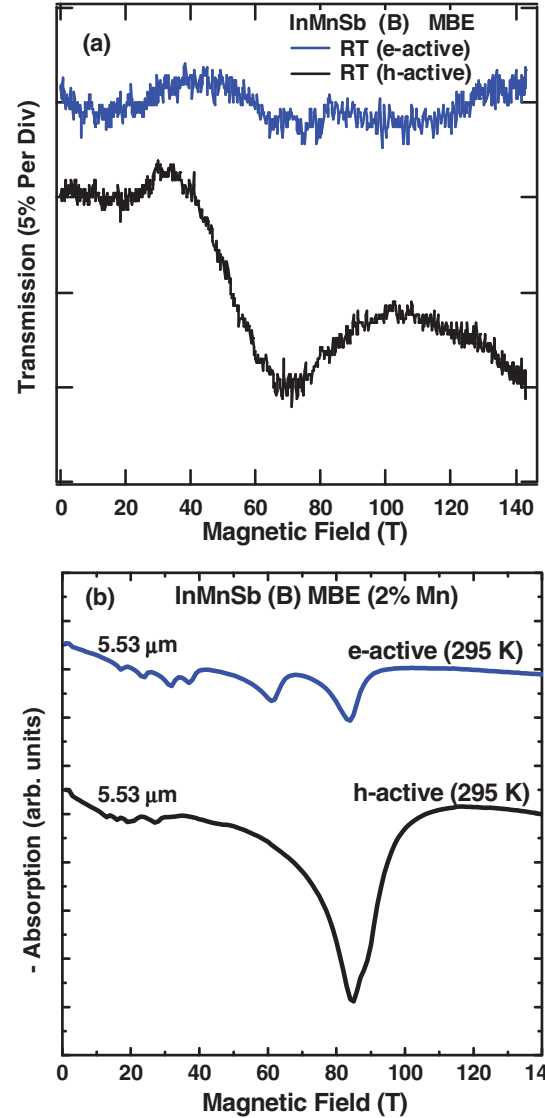


FIG. 10. (Color online) (a) CR with electron and hole active polarization for MBE-grown InMnSb (B). (b) Calculated CR spectra for the MBE-grown InMnSb (B) with the electron-active, demonstrating several transitions in the conduction band, and the hole-active polarization of light.

states which decouple at the zone center, i.e., $k_z = 0$. The Bloch basis states for the upper set are $|S\uparrow\rangle$, $|HH\uparrow\rangle$, $|LH\downarrow\rangle$, and $|SO\downarrow\rangle$, which correspond to electron spin up, heavy-hole spin up, light-hole spin down, and split-off-hole spin down, respectively. Similarly, the Bloch basis states for the lower set are $|S\downarrow\rangle$, $|HH\downarrow\rangle$, $|LH\uparrow\rangle$, and $|SO\uparrow\rangle$ corresponding to electron spin down, heavy-hole spin down, light-hole spin up, and split-off-hole spin up. The explicit expressions for these 8 Bloch basis states are given in Ref. 11. The total effective mass Hamiltonian is the sum of the Landau (H_L), Zeeman (H_Z), and sp - d exchange (H_{ex}) contributions; i.e.,

$$H = H_L + H_Z + H_{ex}. \quad (1)$$

Explicit expressions for these Hamiltonians are given in Ref. 11. We used the standard Luttinger parameters²⁷ and

TABLE II. Measured CR mass and CR mobility (μ_{CR}) for different excitation wavelengths. The μ_{CR} was extracted from the width of the resonance peaks. The measurements for InMnSb (A) at 5.53 μm are not shown here.

Sample	Growth Method	λ (μm)	m^* (m_0)	μ_{CR} [$\text{cm}^2/(\text{V s})$]	Temp (K)	Mn (%)
InMnAs	MOVPE	10.7	0.036	480	295	2
InMnAs	MOVPE	10.7	0.037	600	121	2
InMnSb	MBE	10.6	0.057	500	295	2
InMnSb	MBE	10.7	0.051	700	121	2
InMnAs	MOVPE	5.53	0.046	750	30	4
InMnAs	MOVPE	5.53	0.045	650	40	2
InMnAs	MOVPE	5.53	0.043	400	20	1
InMnSb (A)	MBE	5.53	0.036	400	295	2
InMnSb (A)	MBE	5.53	0.033	500	65	2
InMnSb (B)	MBE	5.53	0.037	400	295	2
InMnSb	MOVPE	5.53	0.035	1000	61	5.6

temperature-dependent energy gaps for InAs and InSb as inputs in the Landau and Zeeman Hamiltonians.

In the Mn exchange Hamiltonian, H_{ex} , of Eq. (1), we follow the method of Kossut²⁸ and include the effects of the spontaneous magnetization of the Mn ions (magnetic impurities) and the coupling of this magnetization to the conduction band electrons and valance band holes through the s - d and p - d exchange interactions, respectively. The values of the exchange constants for the s - d interaction, α , and p - d interaction, β , are taken to be 0.5 eV and -1.0 eV, respectively.²⁹ The spontaneous magnetization depends on the Mn concentration, x , and the z component of the average Mn spin, $\langle S_z \rangle$. The value of x in our calculations is taken to be the actual Mn fraction in the samples. The value of $\langle S_z \rangle$ is determined in the mean-field approximation using the lattice temperature, T , and the Curie temperature, T_c , of the samples as inputs. With the inclusion of ferromagnetic ordering of the Mn ions, the spontaneous magnetization and its sp - d coupling to the itinerant carriers will spin-split the bands even in the absence of an external magnetic field.

B. Effective mass energies and wave functions

Although translational symmetry is broken in the x direction with the choice of the Landau gauge $\vec{A} = B x \hat{y}$, it still holds in the y and z directions. Therefore, k_y and k_z are still good quantum numbers and the envelope functions of the effective mass Hamiltonian, H , in Eq. (1) are given by¹¹

$$\mathcal{F}_{p,v} = \frac{e^{i(k_y y + k_z z)}}{\sqrt{\mathcal{A}}} \begin{bmatrix} C_{p,1,v}(k_z) \phi_{p-1} \\ C_{p,2,v}(k_z) \phi_{p-2} \\ C_{p,3,v}(k_z) \phi_p \\ C_{p,4,v}(k_z) \phi_p \\ C_{p,5,v}(k_z) \phi_p \\ C_{p,6,v}(k_z) \phi_{p+1} \\ C_{p,7,v}(k_z) \phi_{p-1} \\ C_{p,8,v}(k_z) \phi_{p-1} \end{bmatrix}. \quad (2)$$

The complete wave functions are obtained by multiplying these envelope functions by the corresponding $k_z = 0$ Bloch

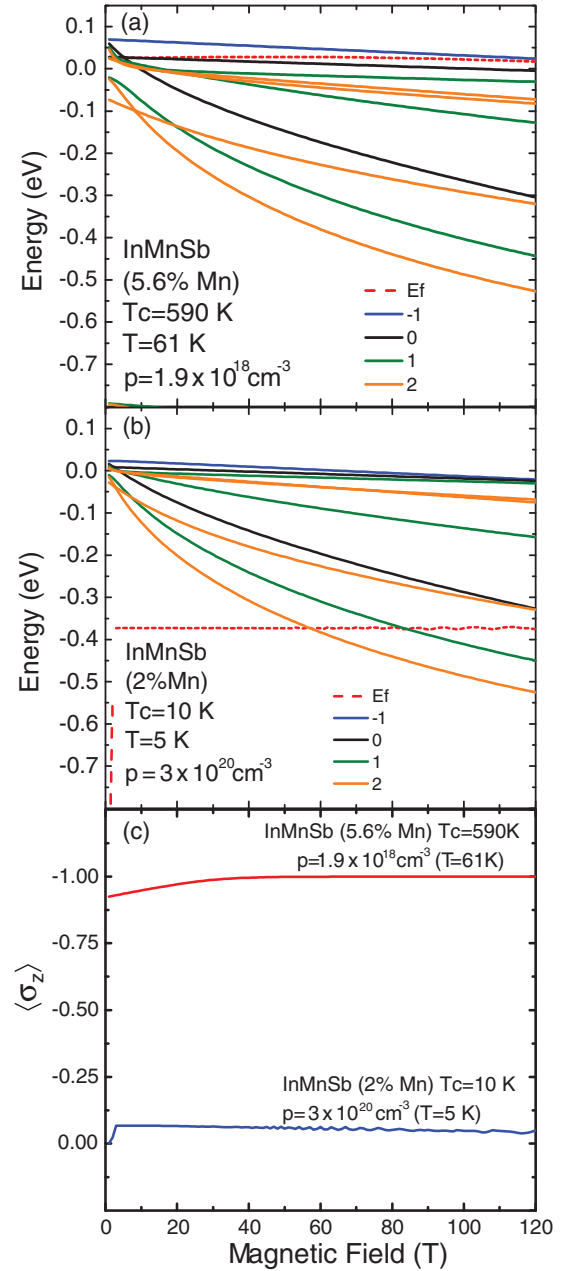


FIG. 11. (Color online) Calculated Landau levels in p -doped $\text{In}_{1-x}\text{Mn}_x\text{Sb}$ for (a) $x = 5.6\%$ (with $T_c = 590$ K and $T = 61$ K) and (b) $x = 2\%$ (with $T_c = 10$ K and $T = 290$ K). The Fermi energies are shown as red dotted line for $p = 1.9 \times 10^{18} \text{ cm}^{-3}$ and $p = 3 \times 10^{20} \text{ cm}^{-3}$. (c) The calculated z component of the average Pauli matrix corresponding to these two different samples demonstrating a much larger average spin for the MOVPE-grown structure with higher Mn content and lower carrier density. This difference could explain the higher T_c in the MOVPE-grown structure.

basis states. In Eq. (2), p is the Pidgeon-Brown (PB) manifold index associated with the Hamiltonian matrix, v labels the eigenvectors within the p th manifold, $\mathcal{A} = L_x L_y$ is the cross-sectional area of the sample in the xy plane, $\phi_i(\xi)$ are harmonic oscillator eigenfunctions evaluated at $\xi = x - \lambda^2 k_y$ where λ is the magnetic length, and $C_{p,q,v}(k_z)$ are complex expansion coefficients ($q = 1 \dots 8$ corresponds to the 8 Bloch basis states) for the v th eigenstate which depends explicitly on p and k_z .

Since the harmonic oscillator part of the wave function ϕ_i for each component in Eq. (2) must have $i \geq 0$, the Pidgeon-Brown manifold index p can take on integer values from $p = -1, 0, 1, 2, \dots$. For the $p = -1$ Pidgeon-Brown manifold, since $n \geq 0$, there is only one allowed nonzero component in the manifold. This is the 6th component ($q = 6$) in Eq. (2) corresponding to heavy-hole spin down. Similarly, the Pidgeon-Brown manifolds for $p = 0, 1$ have four and seven allowed nonzero components. For $p \geq 2$, all PB manifolds have eight allowed nonzero components. Within a given Pidgeon-Brown manifold, for each component in Eq. (2), the sum $n + m_j$ of the oscillator index plus the m_j quantum number for the Bloch part of the state is a constant. In the cylindrical approximation, where the Luttinger parameters satisfy $\gamma_2 = \gamma_3$, optical transitions are only allowed if the Pidgeon-Brown manifold indices p satisfy the selection rule $\Delta p = \pm 1$. This selection rule greatly aids us in determining the states that contribute to a given optical transition.

Substituting the envelope function $\mathcal{F}_{p,v}$ from Eq. (2) into the effective mass Schrödinger equation with H given by Eq. (1), we obtain a set of matrix eigenvalue equations

$$H_p F_{p,v} = E_{p,v}(k_z) F_{p,v} \quad (3)$$

that can be solved for each allowed value of the Pidgeon-Brown manifold index, p , and wave vector, k_z , to obtain the electronic energies and effective mass envelope functions. Since the harmonic oscillator functions, $\phi_i(\xi)$, are only defined for $i \geq 0$, one deletes the rows and columns of H_p for which $i < 0$. It follows from Eq. (2) that $F_{p,v}$ is defined for $p \geq -1$. The resulting eigenvalues are the Landau levels, denoted as $E_{p,v}(k_z)$, where p labels PB manifold and v labels the eigenenergies belonging to the same PB manifold in ascending order.

C. Landau levels, CR spectra, and Fermi energies

We can obtain the Landau levels at the zone center as a function of magnetic field using the energy eigenvalues at wave vector $k_z = 0$. In general, we calculate Landau energy level bands as a function of wave vector, k_z , at a given magnetic field in the z direction, B_z . The *CR absorption spectra* are obtained from the *magneto-optical absorption* due to direct transitions between different Landau levels. From Fermi's golden rule, the *magneto-optical absorption coefficient*, α (not to be confused with the *s-d coupling parameter* α), at the photon energy $\hbar\omega$ for a magnetic field B_z is given by^{11,30}

$$\alpha(\hbar\omega) = \frac{e^3 B_z}{(\hbar\omega)(\hbar c)^2 n_r} \sum_{p,v,p',v'} \int_{-\infty}^{\infty} dk_z |\hat{e} \cdot \vec{P}_{p,v}^{p',v'}(k_z)|^2 \times [f_{p,v}(k_z) - f_{p',v'}(k_z)] \delta(\Delta E_{p,v}^{p',v'}(k_z) - \hbar\omega), \quad (4)$$

where \hat{e} is the unit polarization vector of the incident light, $\vec{P}_{p,v}^{p',v'}(k_z)$ is the optical matrix element for direct transitions between the electronic states (p, v, k_z) and (p', v', k_z) , $\Delta E_{p,v}^{p',v'}(k_z) = E_{p',v'}(k_z) - E_{p,v}(k_z)$ is the corresponding optical transition energy, and n_r is the refractive index. The Fermi distribution function $f_{p,v}(k_z)$ in Eq. (4) is given by

$$f_{p,v}(k_z) = \frac{1}{1 + \exp[(E_{p,v}(k_z) - E_f)/kT]}. \quad (5)$$

The Fermi energy, E_f , in Eq. (5) depends on both the temperature and the net itinerant carrier concentration and also shows a slight dependence on the external magnetic field. The net itinerant carrier concentration, $N_C = n - p$, can be either positive or negative depending on whether the doping of the sample is n type or p type. For a fixed temperature, magnetic field, and Fermi level, the net carrier concentration is

$$N_C = \frac{e B_z}{(2\pi)^2 (\hbar c)} \sum_{p,v} \int_{-\infty}^{\infty} dk_z [f_{p,v}(k_z) - \delta_{p,v}^v], \quad (6)$$

where $\delta_{p,v}^v = 1$ if the (p, v) is a Landau valence subband and $\delta_{p,v}^v = 0$ if (p, v) is a Landau conduction subband. The Fermi energy can be calculated from Eq. (6) using a root finding program for the given values of temperature, net carrier concentration (determined from the experimental Hall effect measurements), and magnetic field.

V. RESULTS AND DISCUSSION

The measured CR mass and mobility for the samples studied in this paper are summarized in Table II. The cyclotron mobilities in Table II, measured from the CR linewidth, are larger than those obtained by dc transport measurements. This is partly because the heavy-hole cyclotron masses in this high-field range are an order of magnitude smaller than their classical value at the band edge. In our ferromagnetic InMnAs samples we observed an increase in the CR mobility at high magnetic fields which is the opposite of the observations in p -type InAs with the hole density $5 \times 10^{18} \text{ cm}^{-3}$ and comparable mobility to the InMnAs structures.¹⁰ One possible origin of this effect could be the reduction of magnetic scattering at high fields, since the randomness of Mn spins decreases at strong magnetic fields even at room temperature. This is consistent with the fact that the relative increase of the mobility compared to the dc value is larger for the ferromagnetic samples compared to the nonmagnetic p -type InAs.¹⁰ This is the first reported observation of CR features in ferromagnetic InMnSb structures and these features are different from the previously reported CR in a nonmagnetic p -type InSb at high magnetic fields.³¹ We also find that the peak linewidths are narrower in the MOVPE-grown samples, indicative of the higher mobilities in these samples. Higher growth temperatures in MOVPE structures could result in lower defects, increasing the mobility.^{7,8}

In our observations, the CR originates only from the transitions in the valence band, suggesting the absence of the midgap impurity states. There can be two effects of the impurity states interacting with the valence band states. The first effect comes from the exchange interaction between the impurity spins and the valence band spins. This effect is included in our model (see Sec. IV and Refs. 22–24,28). The second effect can result from hybridization of the impurity levels with the valence band states. We do not include this hybridization effect in our model, since we have assumed that the impurity states lie deep within the valence bands; hence this hybridization is unimportant for the CR. This might be different for GaMnAs,^{21,32} where the impurity states might lie in the gap or near the edge of the valence band states. We have assumed that the impurity band states lie deep within the valence band and not in the gap or near the edge for InMnAs

and InMnSb because if they did, we should see impurity state CR transitions, which would be distinguished from the valence band CR. Experimentally, impurity band CR is not seen in InMnAs (Ref. 10). Furthermore, the observed valence band CR is fairly accurately reproduced by our model which indicates that either the impurity band is deep within the valence band, or if it is near the edge, the hybridization with the valence band is weak. This may not be the case in GaMnAs, but we noted that CR has not been observed in GaMnAs and this might be a reason for that.

While we find differences in the peak positions of the CR peaks between the MBE and MOVPE samples, these differences can be attributed to the differences in carrier density and hence the position of the Fermi levels in the samples. The change in Fermi level also plays an important part in determining the average z component of the spins. For low doping, the Fermi level lies in the lowest energy (heavy-hole down) valence band which is a pure spin state. At higher doping, the Fermi level lies into the valence bands and several states are occupied and the average spin goes down. As shown in Fig. 11(c) for InMnSb grown by MOVPE with 5.6% Mn content, the lower carrier density in the structure results in a much higher average z component of the spins compared to the MBE-grown structure. This fact could be responsible

for the higher Curie temperature in the MOVPE structures where in this case, the topmost level is a pure spin state from 0–80 T.

In summary, we observed CR in InMnAs and InMnSb based films with different Mn contents at various temperatures to investigate their band structure, carrier states, average spin, and the exchange interaction of conduction and valence band carriers with localized Mn d electrons. Clear observations of CR, in combination with calculations based on an effective mass theory using the exchange parameters $\alpha = -0.5$ eV and $\beta = 1.0$ eV, lead us to the determination of the complex band structure in these ferromagnetic systems. Our observations should be important for designing new spin-based semiconductor devices and provide new insights in the band structure of the ferromagnetic structures.

ACKNOWLEDGMENTS

The work was supported by the NSF through awards DMR-0846834 (Career), DMR-0804479, DMR-1157490 (GDS, CJS) and by the National High Magnetic Field Laboratory (DS), which is supported by National Science Foundation Cooperative Agreement No. DMR-0654118, the State of Florida, and the US Department of Energy.

*Author to whom correspondence should be addressed: khoda@vt.edu

¹H. Munekata, H. Ohno, S. von Molnar, A. Segmuller, L. L. Chang, and L. Esaki, *Phys. Rev. Lett.* **63**, 1849 (1989).

²T. Schallenberg and H. Munekata, *Appl. Phys. Lett.* **89**, 042507 (2006).

³J. Wang, C. Sun, Y. Hashimoto, J. Kono, G. Khodaparast, L. Cywinski, L. J. Sham, G. D. Sanders, C. J. Stanton, and H. Munekata, *J. Phys.: Condens. Matter* **18**, R501 (2006).

⁴K. Sato, L. Bergqvist, J. Kudrnovsky, P. H. Dederichs, O. Eriksson, I. Turek, B. Sanyal, G. Bouzerar, H. Katayama-Yoshida, V. A. Dinh, T. Fukushima, H. Kizaki, and R. Zeller, *Rev. Mod. Phys.* **82**, 1633 (2010).

⁵T. Wojtowicz, G. Cywinski, W. L. Lim, X. Liu, M. Dobrowolska, J. K. Furdyna, K. M. Yu, W. Walukiewicz, G. B. Kim, M. Cheon, X. Chen, S. M. Wang, and H. Luo, *Appl. Phys. Lett.* **82**, 4310 (2003).

⁶T. Wojtowicz, W. L. Lim, X. Liu, G. Cywinski, M. Kutrowski, L. V. Titova, K. Yee, M. Dobrowolska, J. K. Furdyna, K. M. Yu, W. Walukiewicz, G. B. Kim, M. Cheon, X. Chen, S. M. Wang, H. Luo, I. Vurgaftman, and J. R. Meyer, *Physica E* **20**, 325 (2004).

⁷A. J. Blattner and B. W. Wessels, *Appl. Surf. Sci.* **221**, 155 (2004).

⁸N. Rangaraju, P. Li, and B. W. Wessels, *Phys. Rev. B* **79**, 205209 (2009).

⁹N. D. Parashar, N. Rangaraju, V. K. Lazarov, S. Xie, and B. W. Wessels, *Phys. Rev. B* **81**, 115321 (2010).

¹⁰Y. H. Matsuda, G. A. Khodaparast, M. A. Zudov, J. Kono, Y. Sun, F. V. Kyrychenko, G. D. Sanders, C. J. Stanton, N. Miura, S. Ikeda, Y. Hashimoto, S. Katsumoto, and H. Munekata, *Phys. Rev. B* **70**, 195211 (2004).

¹¹G. D. Sanders, Y. Sun, F. V. Kyrychenko, C. J. Stanton, G. A. Khodaparast, M. A. Zudov, J. Kono, Y. H. Matsuda, N. Miura, and H. Munekata, *Phys. Rev. B* **68**, 165205 (2003).

¹²G. A. Khodaparast, J. Kono, Y. H. Matsuda, S. Ikeda, N. Miura, Y. J. Wang, T. Slupinski, A. Oiwa, H. Munekata, Y. Sun, F. V. Kyrychenko, G. D. Sanders, and C. J. Stanton, *Physica E* **21**, 978 (2004); in this study, the holes at the interface layer of InMnAs and GaSb could have contributed to the observed CR.

¹³E. J. Singley, R. Kawakami, D. D. Awschalom, and D. N. Basov, *Phys. Rev. Lett.* **89**, 097203 (2002).

¹⁴K. Hirakawa, S. Katsumoto, T. Hayashi, Y. Hashimoto, and Y. Iye, *Phys. Rev. B* **65**, 193312 (2002).

¹⁵Y. Nagai, T. Kunimoto, K. Nagasaka, H. Nojiri, M. Motokawa, F. Matsukura, T. Dietl, and H. Ohno, *Jpn. J. Appl. Phys.* **40**, 6231 (2001).

¹⁶A. M. Yakunin, A. Y. Silov, P. M. Koenraad, J. H. Wolter, W. Van Roy, J. DeBoeck, J.-M. Tang, and M. E. Flatte, *Phys. Rev. Lett.* **92**, 216806 (2004).

¹⁷K. Hirakawa, A. Oiwa, and H. Munekata, *Physica E* **10**, 215 (2001).

¹⁸M. Bhowmick, T. R. Merritt, G. A. Khodaparast, B. W. Wessels, S. A. McGill, D. Saha, X. Pan, G. D. Sanders, and C. J. Stanton, *Phys. Rev. B* **85**, 125313 (2012).

¹⁹G. A. Khodaparast, M. Bhowmick, C. Feeser, B. W. Wessels, D. Saha, G. D. Sanders, and C. J. Stanton, *Proc. SPIE* **8461**, 846110 (2012).

²⁰Y. H. Matsuda, G. A. Khodaparast, R. Shen, S. Takeyama, X. Liu, J. Furdyna, and B. W. Wessels, *J. Phys.: Conf. Ser.* **334**, 012056 (2011).

²¹M. Dobrowolska, K. Tivakornsasithorn, X. Liu, J. K. Furdyna, M. Berciu, K. M. Yu, and W. Walukiewicz, *Nature Materials* **11**, 444 (2012).

²²G. D. Sanders, Y. Sun, C. J. Stanton, G. A. Khodaparast, J. Kono, Y. H. Matsuda, N. Miura, T. Slupinski, A. Oiwa, and H. Munekata, *J. Appl. Phys.* **93**, 6897 (2003).

- ²³G. D. Sanders, Y. Sun, C. J. Stanton, G. A. Khodaparast, J. Kono, Y. H. Matsuda, N. Miura, T. Slupinski, A. Oiwa, and H. Munekata, *J. Supercond.* **16**, 449 (2003).
- ²⁴Y. Sun, G. D. Sanders, F. V. Kyrychenko, C. J. Stanton, G. A. Khodaparast, J. Kono, Y. H. Matsuda, N. Miura, and H. Munekata, *Physica E* **20**, 374 (2004).
- ²⁵G. D. Sanders, Y. Sun, C. J. Stanton, G. A. Khodaparast, J. Kono, D. S. King, Y. H. Matsuda, S. Ikeda, N. Miura, A. Oiwa, and H. Munetaka, *Physica E* **20**, 378 (2004).
- ²⁶C. K. Pidgeon and R. N. Brown, *Phys. Rev.* **146**, 575 (1966).
- ²⁷I. Vurgaftman, J. R. Meyer, and L. R. Ram-Mohan, *J. Appl. Phys.* **89**, 5815 (2001).
- ²⁸J. Kossut, *Semicond. Semimet.* **25**, 183 (1988).
- ²⁹M. A. Zudov, J. Kono, Y. H. Matsuda, T. Ikaida, N. Miura, H. Munekata, G. D. Sanders, Y. Sun, and C. J. Stanton, *Phys. Rev. B* **66**, 161307(R) (2002).
- ³⁰F. Bassani and G. P. Parravicini, *Electronic States and Optical Transitions in Solids* (Pergamon, New York, 1975).
- ³¹C. L. Littler, D. G. Seiler, R. Kaplan, and R. J. Wagner, *Phys. Rev. B* **27**, 7473 (1983).
- ³²B. C. Chapler, S. Mack, R. C. Myers, A. Frenzel, B. C. Pursley, K. S. Burch, A. M. Dattelbaum, N. Samarth, D. D. Awschalom, and D. N. Basov, *Phys. Rev. B* **87**, 205314 (2013).